Broken Rotor Bar Fault Detection of Induction Machine Based on Rectified Orthogonal Axes of Stator Current

Saeed Hajnayeb, Mohammad Hoseintabar Marzebali, Vahid Abolghasemi, *Senior Member*, *IEEE,*
Jawad Faiz*, Senior Member*, *IEEE*

***Abstract*— In induction machines (IMs), the characteristic frequency of broken rotor bars (BRB) shows modulations by the fundamental frequency, appearing as sidebands in the motor current signature, and often suffering from frequency leakage. This leakage can obscure fault components, potentially leading to catastrophic motor failure. Effective frequency demodulation must separate fault frequency sidebands from the fundamental frequency, eliminate nearby harmonics, and maintain the fault characteristic amplitude while considering the number of measured phases. To address these challenging tasks, we propose a novel method based on the rectified orthogonal axis technique (ROAT), applied to the stator current. The proposed method preserves the amplitudes of the fault characteristic frequency while transferring the energy of the fundamental frequency to the DC value and the 4th harmonic of the supply frequency ($4f_s$). This frequency shift is crucial for fault diagnosis in inverter-fed induction machines, particularly at low speeds. Our extensive simulations and experiments on motors with several broken rotor bars under single and three-phase conditions demonstrate the high efficiency and performance of the proposed approach.**

***Index Terms*— Induction motor, Broken rotor bar fault detection, Fault diagnosis, Motor current signal analysis.**

NOMENCLATURE

f_s	Supply frequency.
f_m	Sampling frequency.
f_{BRB}	Broken rotor bar fault characteristic frequency.
s	Slip.
β	Severity of broken rotor bar fault.
I	Maximum amplitude of stator current.
i(t)	Stator current.
H(.)	Hilbert transform.
h	Number of harmonics.
FT(.)	Fourier Transform.
δ(.)	Dirac delta function.
Env[.]	Envelope function.
$\omega(t)$	Instantaneous angular frequency.
$A(t)$	Instantaneous amplitude frequency.
n	Rotational speed.
p	Number of poles.
$\vec{i}_{PV}$	Clarke vector of stator current.

I. Introduction

INDUCTION machines (IMs) are widely recognized as the most popular and extensively used machines in industry due to their simplicity, cost-effectiveness, reliability, and high strength [1-3]. Consequently, condition monitoring of motors to detect faults and prevent unplanned shutdowns, reduce repair and maintenance costs, and minimize downtime, is crucial. Failures of IMs can arise from faults in various components including the stator, rotor, motor's mechanical system (such as bearings and shaft), or other sources [4, 5]. Rotor cage faults account for approximately 10% of all faults [6, 7].

Failure of rotor bars leads to oscillations in rotor speed and torque, accelerating fatigue on bearings. A broken rotor bar (BRB) reduces the efficiency and reliability of the motor, limiting its ability to develop the required torque. Failure to recognize such faults promptly may cause severe damage to the machine [4], [8-11]. Therefore, monitoring and early detection of BRBs are essential. Theoretical analysis comparing a healthy rotor to one with BRBs reveals that current passing the bars creates a three-phase magnetic field rotating at the slip frequency (sf_s). In a healthy rotor, there is only a forward-rotating field at the sf_s. In the case of BRBs, a backward-rotating generates magnetic field at the $-sf_s$, which induces an electromotive force (EMF) in the stator winding. This creates components in the stator current signatures at frequencies of $(1\pm2s)f_s$, which emerge as sidebands around the supply frequency (f_s) [12, 13].

There are various condition monitoring techniques based on mechanical an electrical signature, such as vibration, temperature, noise/acoustic ratio, noise, speed fluctuation, magnetic flux, and motor current signature analysis (MCSA) [14]. Monitoring of temperature, vibration, and magnetic flux are invasive techniques and needs extra sensors. These techniques are costly and have some drawbacks such as the need for motor disassembly, which is time-consuming, and labor-intensive. Furthermore, invasive techniques may require specialized equipment and expertise, making them less accessible or practical for routine monitoring tasks. Non-invasive techniques, such as MCSA, do not impact the internal design of the motor [10]. In recent years, MCSA has gained more attention due to its cost-effectiveness, elimination of additional hardware complexity, and non-alteration of the motor structure. Moreover, MCSA can analyze BRBs, cracked end rings, stator faults, misalignment, and bearing failures [14]. Most MCSA approaches are based on detecting sideband frequencies around the fundamental frequency. The fast Fourier transform (FFT) is a common technique for MCSA, mainly

used for steady-state operations to detect BRBs in IMs. However, FFT suffers from spectral leakage; the amplitude of the principal component is much higher than that of the fault harmonics, causing them to be concealed [10]. Several approaches have been introduced to overcome the leakage problem, such as eliminating the principal component through notch and Kalman filters [15, 16]. Nevertheless, these methods require knowledge of noise and may attenuate fault harmonics. Other approaches have been introduced to avoid the principal component leakage problem, which is based on converting the principal component of the current to a DC component. These techniques mitigate leakage in the discrete FT (DFT) spectrum, such as envelope analysis (EA) based on Hilbert transform (HT) [17], analysis of the rectified motor current [18], Teager-Kaiser energy operator (TKEO) [19], third-order energy operator (TOEO) [20, 21], square current spectrum analysis (SCSA) [22], enhanced phase vector analysis (EPVA) [23], sum of adjacent products (SAP) [24] and frequency domain energy operator (FDEO) have been introduced [25]. Although these approaches solve the leakage problem, they have their drawbacks. For example, SAP and SCSA alter the magnitude of fault frequency characteristics, and EPVA and SAP uses three current sensors. TKEO has phase distortion due to require causal processing, and hence, Li *et al*. has proposed FDEO to overcome this issue [26]. However, it has been shown that FDEO cannot properly identify fault features under light load conditions due to strong noise contamination and frequency component interference [1]. Therefore, normalized frequency domain energy operator (NFDEO) was proposed to increase the capability of detecting BRB fault under light load conditions [1].

In inverter-fed motors, the fundamental frequency may vary within a very wide range. Consequently, the corresponding frequency components also change considerably under different conditions, presenting a challenge in detecting BRB fault. Although the fault characteristic amplitude is not identical at different speeds, it increases with decreasing motor speed. However, the fault characteristic frequency ($2sf_s$) remains constant under a constant torque load, while the slip increases with decreasing frequency [27-32]. Therefore, demodulation methods are suitable for detecting the fault characteristic frequency. It is worth mentioning that demodulation techniques work by transferring the fundamental harmonic to the DC value and other harmonics. In the existing rectification methods, the fault characteristic frequency is maintained at its actual value, while the energy of the main harmonic (f_s) is normally transferred to the DC value and to the second harmonic ($2f_s$). Nevertheless, when the supply frequency is small, the proximity between the fault's characteristic frequency and the harmonic of the supply frequency would be very small [34-36].

This paper proposes a novel approach, termed rectified orthogonal axes technique (ROAT), employs the Hilbert transform to create a virtual signal with a phase shifted by 90º relative to the original signal (called orthogonal axes). The original and virtual signals are then rectified, leading to the elimination of the fundamental frequency leakage. In the proposed approach, frequency components are created as a DC part, fault characteristic harmonics $2sf_s$, $4f_s$, and sideband frequency components. As a result, the fault characteristic frequency of $2sf_s$ is placed far away from the frequency of $4f_s$. It is worth noting that, ROAT can be easily adapted from single-phase (S-ROAT) case to the three-phase (T-ROAT) case.

The rest of the paper is organized as follows. Section II provides a mathematical description of the BRB faults. Section III presents mathematical and theoretical definitions of the proposed method and synthetic signal for validation. Section IV presents the experimental results to validate the proposed method. Finally, Section V concludes the paper.

II. Broken rotor bar fault

When a bar in the rotor cage fractures, it creates an anti-rotational magnetic field within the rotor that is opposite to the main rotating magnetic field. Due to the mechanical speed of this machine, it causes the stator to have a current with a frequency of $(1\pm2s)f_s$, which appears as sidebands around the fundamental frequency. Leakage of the fundamental frequency results in hidden sidebands. Therefore, demodulation techniques need to be used as pre-processing stage to reduce leakage and separate the characteristic frequencies of BRBs. In this section, the impact of BRB on the stator current signature with simplified mathematical equations as well as different demodulation techniques are described.

A. Mathematical modeling of BRB

A BRB fault modulates amplitude of the stator current, with the following frequencies:

$$f_{BRB} = 2ksf_s. \qquad k = 1, 2, 3, \ldots \tag{1}$$

The stator phase current in an IM with a BRB fault is as follows [37]:

$$i(t) = I\cos\left(2\pi f_s t\right)\left(1+\beta\cos\left(2\pi f_{BRB} t\right)\right). \tag{2}$$

Considering the first main harmonic component (k = 1) given in (1), (2) can be simplified as follows:

$$i(t) = I\cos(2\pi f_s t) + \frac{\beta}{2} I\cos(2\pi f_s(1-2s)t) + \frac{\beta}{2} I\cos(2\pi f_s(1+2s)t), \tag{3}$$

where the fault characteristic frequency, which emerges as sidebands of the fundamental component, are $f_s \pm 2sf_s$. Since different demodulation techniques are used for fault detection process in MCSA, these techniques are investigated in the next section to show the characteristics of each method, separately. This allows a clear identification of advantages and disadvantages of each method, collectively.

B. Fault diagnosis demodulation techniques

1) Rectified stator current

The spectrum of the rectified stator current is simply realized, either by taking the absolute value (|.|) of $i(t)$, or by rectifying it using a diode bridge in practice [18]. The mathematical definition of rectified signal is given as follow:

$$|i(t)| = i(t) \times \text{sgn}(\cos(2\pi f_s t)), \tag{4}$$

where:

$$\text{sgn}(\cos(2\pi f_s t)) = \frac{4}{\pi} \sum_{h=1,3,5,..}^{\infty} \left[\frac{\sin(h\frac{\pi}{2})}{h} \cos(h2\pi f_s t) \right], \tag{5}$$

$$|i(t)| \approx \frac{4}{\pi}\frac{I}{2}\left(1 + \beta\cos(2\pi(2sf_s)t)\right), \tag{6}$$

$$FT\{i(t)\}(f) = |i(t)|(f) = \frac{4}{\pi}\frac{I}{2}\left(1 \times \delta(f) + \frac{\beta}{2} \times \delta(f - 2sf_s)\right) \tag{7}$$

$$|i(t)|(f)|_{dB} = 0 \times \delta(f) + 20\log(\frac{\beta}{2}) \times \delta(f - 2sf_s), \tag{8}$$

$$|i(2sf_s)|_{dB} = 20\log(\frac{\beta}{2}). \tag{9}$$

2) Squared current signal

The squared current for an IM with a BRB fault can be mathematically expressed as [22]:

$$i^2(t) = \frac{I^2}{2}((1 + 2\beta^2) + 2\beta\cos(2\pi(2sf_s)t) + \\ + \beta I^2 \cos(4\pi(2sf_s)t)), \tag{10}$$

$$i^2(2sf_s)|_{dB} = 20\log(\frac{\beta}{1 + 2\beta^2}) \approx 20\log(\beta). \tag{11}$$

3) Extended Park's Vector Approach (*EPVA*)

EPVA method requires all three currents of a motor [23] as follows:

$$\vec{i}_{PV}(t) = i_D(t) + ji_Q(t), \tag{12}$$

where

$$i_D(t) = \frac{\sqrt{2}}{\sqrt{3}} i_a(t) - \frac{1}{\sqrt{6}} i_b(t) - \frac{1}{\sqrt{6}} i_c(t), \tag{13}$$

$$i_Q(t) = \frac{1}{\sqrt{2}} i_b(t) - \frac{1}{\sqrt{2}} i_c(t). \tag{14}$$

This method includes DC and low frequency components as follows:

$$\left|\vec{i}_{PV}\right| = \left|i_D(t) + ji_Q(t)\right| = \frac{\sqrt{3}}{\sqrt{2}} I(1 + \beta\cos(2\pi(2sf_s)t)). \tag{15}$$

The fault severity is as follows:

$$\left|i_{PV}\right|(2sf_s)\Big|_{dB} = 20\log(\frac{\beta}{2}). \tag{16}$$

4) Teager-Kaiser Energy Operator (*TKEO*)

The energy operator was primarily proposed by Teager and then improved by Kaiser, which is expressed in two continuous and discontinuous modes. It can be used for fault detection by current signal [19]:

$$TKEO\{i(t)\} = i_{TK}(t) = i'(t)^2 - i(t)i''(t). \tag{17}$$

The $TKEO\{i(t)\}$ signal contains a DC component and a low-frequency fault harmonic at a frequency of $2sf_s$

$$i_{TK}(t) = (2\pi f_s I)^2(1 + (1 + s^2)2\beta\cos(2\pi(2sf_s)t)), \tag{18}$$

$$i_{TK}(2sf_s)\Big|_{dB} = 20\log((1 + s^2)\beta) \approx 20\log(\beta). \tag{19}$$

5) Third-Order Energy Operator (*TOEO*)

This method can be used for fault diagnosis of low frequency BRB operating under different constant loads and different supply frequencies. However, this method suffers from noise due to higher-order derivatives [20, 21].

$$TOEO\{i(t)\} = i_{TO}(t) = i'(t)i''(t) - i(t)i'''(t). \tag{20}$$

Discrete sampling sequences of (20) can be written as follows:

$$i_{TO}[n] = i[n]i[n+1] - i[n-1]i[n+2]. \tag{21}$$

6) Frequency Domain Energy Operator (*FDEO*)

This energy operator does not need causal processing and uses corresponding HT; therefore, phase distortion is avoided [25]. Assuming the current signal denoted by $i(t)$, then:

$$Env[i(t)] = i(t) + H(i(t)). \tag{22}$$

The Env[.] of $i'(t)$ is obtained from the following equation.

$$Env[i'(t)] \sim [-\omega(t)A(t)]^2, \tag{23}$$

where

$$A(t) = \sqrt{Env[i(t)]}, \\ \omega(t) = \sqrt{\frac{Env[i'(t)]}{Env[i(t)]}}. \tag{24}$$

7) Sum of Adjacent Products (*SAP*)

The sum of adjacent products (SAP) consists of the sum of the products of every two-adjacent phase current, for a three-phase IM [24]:

$$i_{SAP}(t) = [i_a(t) \quad i_b(t) \quad i_c(t)] \times \begin{bmatrix} i_b(t) \\ i_c(t) \\ i_a(t) \end{bmatrix} \\ = i_a(t)i_b(t) + i_b(t)i_c(t) + i_c(t)i_a(t). \tag{25}$$

Under ideal conditions, i.e. for a healthy three-phase IM, contains only a DC component (26), however in case of faulty IM the (25) can be written as (27).

$$i_{SAP} = -\frac{3}{4} I^2, \tag{26}$$

$$i_{SAP} = 3I(I_l + I_r)\cos(2s(2\pi f_s)t + \frac{2\pi}{3}) + 3I_l I_r \cos(4s(2\pi f_s)t + \frac{2\pi}{3}) - \frac{3}{4} I^2 - \frac{3}{4} I_l^2 - \frac{3}{4} I_r^2 . \tag{27}$$

where I_l and I_r are amplitudes of the fault frequencies on the left and right sides, respectively. According to Eq. (27), a faulty IM with a BRB includes a DC value, and two new fault terms located at $2sf_s$ and $4sf_s$.

The spectrum of a synthetic signal (2) under the faulty condition using above-mentioned methods are illustrated in Fig. 1. The selected parameters for (2) with corresponding reasoning are explained as follows. The value of β was empirically chosen as 0.01, which corresponds to a severe fault of 3 BRB. This value was obtained based on the type and size of motor used in our lab (further detail provided in Section IV). The values for slip (s) were selected as 0.004 and 0.05 to ensure resembling the no-load and full-load conditions, respectively. The supply frequency f_s = 50 Hz considered since the power grid operates at a frequency of 50 Hz. Consequently, is obtained based on $f_{BRB} = 2sf_s$ [38]. According to Fig. 1, and Eq. (11) and Eq. (19), the TKEO and square methods amplify fault characteristics. Conversely, as indicated by Eq. (9), and Eq. (16), and Fig. 1, the Rectified and EPVA methods do not alter fault characteristics. However, the EPVA method requires three current sensors for implementation.

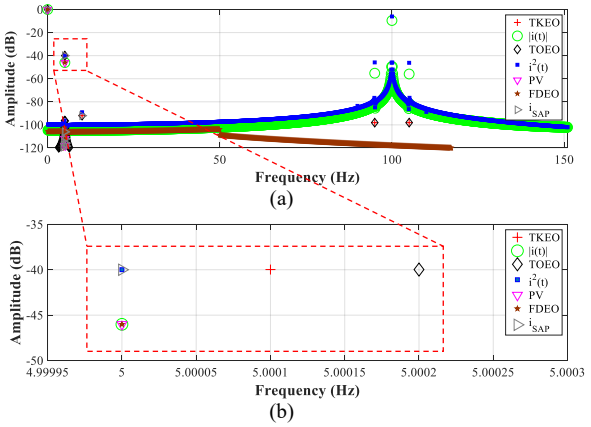

Fig. 1. Comparison of the main fault harmonics generated by different demodulation methods, using a synthetic current of a faulty machine, with f_s = 50 Hz, s = 0.05, and β = 0.01, for the duration of 10 s with f_m= 10 kHz.
+ TKEO method, ○ Rectified current signal method, ▽ EPVA method, ■ square current signal method, ◇ TOEO method, ★ FDEO method, ▷ SAP method.

III. Proposed Method

The proposed method effectively generates a characteristic fault frequency with an amplitude identical to that of the original current signal, preserving the amplitudes of the fault harmonics with a single current sensor. In addition, the method generates a harmonic with a fundamental frequency of $4f_s$, which is significantly distant from the characteristic fault frequency ($2sf_s$). This approach ensures accurate fault detection without distorting the signal or introducing interference with the fault characteristic frequency. In the next section, the characteristics of the HT will be explained, followed by the algorithm of the proposed method. Finally, analytical validation will be conducted to demonstrate the effectiveness of the proposed method.

A. *Hilbert transform* (*HT*)

The HT is a well-known transform, which can be used in the detection of mechanical and electrical faults in IMs. Mathematically, the HT of $i(t)$ is obtained by calculating the convolution between function ($1/\pi t$) and the main signal ($i(t)$) as follows:

$$HT(i(t)) = \frac{1}{\pi t} \times i(t) = \frac{1}{\pi} \int_{-\infty}^{+\infty} \frac{i(\tau)}{(t-\tau)} d\tau. \tag{28}$$

The key property of the HT which offer a deep physical insight can be highlighted as follows [39]. The HT of a trigonometric function $i(t)$ represents a version of itself with a 90º phase shift, i.e., *sines* are transformed to *cosines*, and vice versa. The spectrum of a signal after undergoing the HT retains the same amplitude and frequency contents as the original one. However, the phase of each frequency component is shifted by 90º.

B. *Single Phase Rectified Orthogonal Axes Technique* (*S-ROAT*)

The proposed S-ROAT is designed to shift the main harmonic away from the characteristic fault frequency. The objective of this approach is to generate two orthogonal signals with a phase difference of 90º. Consequently, the upper envelope formed by these signals comprises the fault characteristic frequency at $2sf_s$, along with the harmonic at the $4f_s$. This innovative technique not only effectively separates the fault characteristic from the main harmonic but also ensures enhanced fault detection accuracy by mitigating interference between these frequencies.

Due to significant advancements in the drive industry in recent years, electric machines powered by inverters have gained considerable attention as an attractive and notable option [33]. The impacts of fault in the spectrum of current signature of IMs at different supply frequencies can be depicted as Fig.2 where f_s varies from 50Hz to 20Hz. In inverter-fed IMs, as the supply frequency decreases, the corrsponding supply frequency in the spectrum will move toward to the demudulated fault charectristc frequency (Fig.3). Due to the substantial difference in magnitude between the fundamental harmonics and the characteristic frequency of the BRB, the characteristic frequency of the BRB cannot be properly distinguished. To address this issue, the proposed method shifts the fundamental harmonic by $4f_s$, which improves the detection of the BRB's characteristic frequency, especially at low speeds.

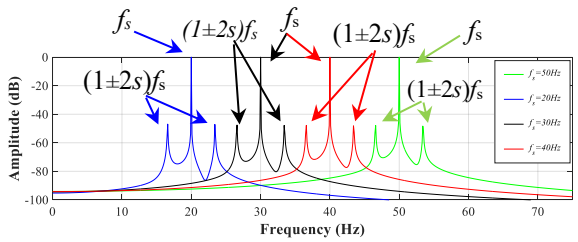

Fig.2. Current spectrum of the inverter-fed IMs at different supply frequencies by changing the frequency [25].

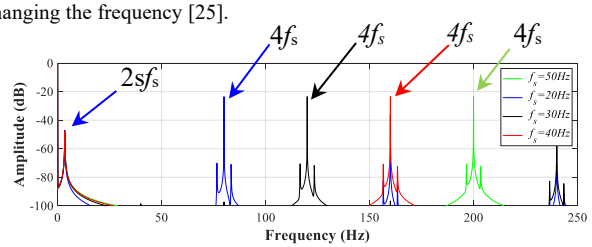

Fig. 3. Decreasing the fundamental frequency and increasing slip with constant fault characteristic frequency (green line $p = 4$, $f_s = 50$, $s = 0.034$ and $n = 1500$ rpm), (red line $p = 4$, $f_s = 40$, $s = 0.042$ and $n = 1200$ rpm), (black line $p = 4$, $f_s = 30$, $s = 0.057$ and $n = 900$ rpm) and (blue line $p = 4$, $f_s = 20$, $s = 0.085$ and $n = 600$ rpm).

A detailed mathematical description of the proposed method is provided as follows.

1) Analytical validation

To analytically implement and analyze the proposed method in this paper, the HT technique is employed [31]. Combining (2) and (4) can result in:

$$H\left(i(t)\right) = I\sin\left(2\pi f_s t\right)\times\left(1+\beta\sin\left(2\pi f_{BRB} t\right)\right), \tag{29}$$

where

$$H\left(i(t)\right) = I\sin(2\pi f_s t) + \frac{\beta}{2} I\sin(2\pi f_s(1-2s)t) + \ldots \\ \ldots \frac{\beta}{2} I\sin(2\pi f_s(1+2s)t). \tag{30}$$

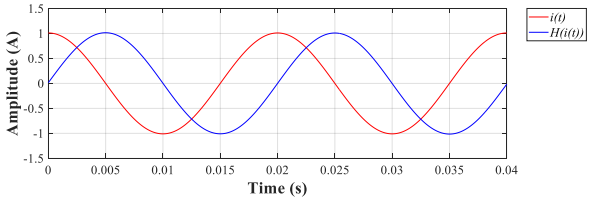

Fig.4. Main signal ($i(t)$) and HT signal ($H(i(t))$).

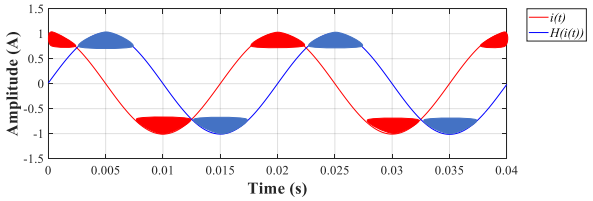

Fig.5. Peak of the main signal (red) and peak of the HT($i(t)$) is (blue).

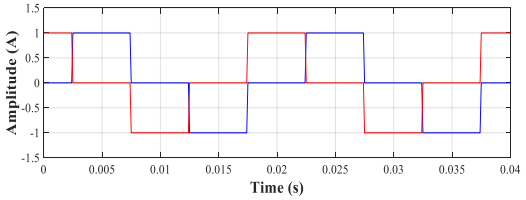

Fig. 6. Square signals for considering of peak sinusoidal signals. Blue: $H(i(t))$ and Red: $i(t)$, mathematically represented as (31) and (32), respectively.

Fig. 4 illustrates the original signal along with result of HT which shows a 90º shift. In the proposed method, only the peaks of the signals should be considered, as highlighted in Fig. 5. The mathematical description of these regions is obtained through modeling the curves in Fig. 6 which can be calculated as *sign* functions given below.

$$sgn(i(t)) = \frac{1}{2}\text{sgn}(\cos(2\pi f_s t - \frac{\pi}{4}) - \cos(2\pi f_s t - \frac{3\pi}{4})), \tag{31}$$

$$sgn(H(i(t)) = \frac{1}{2}\text{sgn}(\cos(2\pi f_s t - \frac{\pi}{4}) + \cos(2\pi f_s t - \frac{3\pi}{4})). \tag{32}$$

where:

$$\text{sgn}(x) = \begin{cases} -1, & if \quad x < 0 \\ 0, & if \quad x = 0. \\ 1, & if \quad x > 0 \end{cases} \tag{33}$$

Eq. (31) and Eq. (32) can be expressed as:

$$\left[\frac{1}{2}\text{sgn}(\cos(2\pi f_s t - \frac{\pi}{4}) - \cos(2\pi f_s t - \frac{3\pi}{4}))\right] = \ldots \\ \ldots \frac{4}{\pi}\times\frac{1}{2}\sum_{h=1,3,5,\ldots}^{\infty}\left[\begin{array}{l} \dfrac{\sin\left(h\frac{3\pi}{4}\right)}{h}\cos\left(h2\pi f_s t\right)+.. \\ \ldots+\dfrac{\sin\left(h\frac{\pi}{4}\right)}{h}\cos\left(h2\pi f_s t\right) \end{array}\right], \tag{34}$$

$$\left[\frac{1}{2}\text{sgn}(\cos(2\pi f_s t - \frac{\pi}{4}) + \cos(2\pi f_s t - \frac{3\pi}{4}))\right] = \ldots \\ \ldots \frac{4}{\pi}\times\frac{1}{2}\sum_{h=1,3,5,\ldots}^{\infty}\left[\begin{array}{l} \dfrac{\cos\left(h\frac{\pi}{4}\right)}{h}\sin\left(h2\pi f_s t\right)+\ldots \\ \ldots+\dfrac{\cos\left(h\frac{3\pi}{4}\right)}{h}\sin\left(h2\pi f_s t\right) \end{array}\right]. \tag{35}$$

By multiplying $i(t)$ and $H(i(t))$ with their corresponding *sgn* counterparts the following equations are derived:

$$\left|i(t)\right| = i(t)\times\text{sgn}(i(t)), \tag{36}$$

$$\left|\hat{i}(t)\right| = H\left(i(t)\right)\times\text{sgn}(H(i(t)). \tag{37}$$

Finally, the i_{ROAT} is obtained through:

$$\left|i_{ROAT}(t)\right| = \left|i(t)\right| + \left|\hat{i}(t)\right|. \tag{38}$$

Eq. (38) can be expanded by considering (36) and (37) as follows:

$$\left|i_{ROAT}(t)\right| = \frac{I\sqrt{2}}{3\pi}\times \times \sum_{h=1,3,5,..}^{\infty} \left\{ \begin{array}{l} \left[\left[\left(\begin{array}{l} \frac{\sin\left(h\frac{3\pi}{4}\right)}{h}\cos\left(h2\pi f_s t\right)+ \\ +\frac{\sin\left(h\frac{\pi}{4}\right)}{h}\cos\left(h2\pi f_s t\right) \end{array} \right)\times .. \right] + ... \right. \\ \left. ... + \left[\left(\begin{array}{l} \frac{\cos\left(h\frac{3\pi}{4}\right)}{h}\sin\left(h2\pi f_s t\right)+ \\ +\frac{\cos\left(h\frac{\pi}{4}\right)}{h}\sin\left(h2\pi f_s t\right) \end{array} \right)\times .. \right] \right\}, \quad (39)$$

$$..\times\left(\cos(2\pi f_s t)\right) \qquad ...\times\left(\sin(2\pi f_s t)\right)$$

For $h = 1$, the above equation can be simplified as:

$$\left|i_{ROAT}(t)\right| = \frac{I\sqrt{2}}{3\pi}\left\{ \begin{array}{r} 6+6\beta\cos(2\pi(2sf_s)t)+2\cos\left(2\pi(4f_s)t\right)+ \\ \beta\cos\left(2\pi(2f_s(2\pm s)t)\right) \end{array} \right\}. \quad (40)$$

It is observed from (40) that $|i_{ROAT}(t)|$ is composed of the following four key components:

- DC component: $\frac{I2\sqrt{2}}{\pi}$.
- Characteristic frequency component: $\frac{I\beta 2\sqrt{2}}{\pi}\cos(2\pi(2sf_s)t)$.
- Fourth harmonic of the fundamental frequency: $\frac{I\beta 2\sqrt{2}}{3\pi}\cos\left(2\pi(4f_s)t)\right)$.
- Sidebands around the fourth harmonic.

Considering the first two terms in (40):

$$\left|i_{ROAT}(t)\right| = \frac{I\sqrt{2}}{3\pi}\left(6+6\beta\cos(2\pi(2sf_s)t\right). \quad (41)$$

The Fourier transform of above equation is given as follows:

$$FT\left\{i_{ROAT}(t)\right\}(f) = \frac{I2\sqrt{2}}{\pi}\left(1\times\delta(f)+\frac{\beta}{2}\times\delta(f-2sf_s)\right). \quad (42)$$

Eq. (42) in the decibel scale can be written as follows:

$$FT\left\{i_{ROAT}(t)\right\}(f)\Big|_{dB} = 0\times\delta(f)+20\log(\frac{\beta}{2})\times\delta(f-2sf_s). \quad (43)$$

The amplitude of fault characteristic frequency component in dB can be calculated as:

$$\left|\hat{i}\left|(2sf_s)\right|\right._{dB} = 20\log(\frac{\beta}{2}). \quad (44)$$

The pseudo of the proposed ROAT for implementation on synthetic and experimental signals is given in Algorithm I.

Algorithm I: ROAT

Input: the current signal y(t), $t = 0, 1, \cdots, N-1$;
Apply Hilbert transform: $H(y(t))$
A = abs [$(y(t))$]
B = abs [$H(y(t))$]
  for $k = 1$ to N do
    if $(A_k > B_k)$
      $C_k = A_k$
    elseif $(B_k >= A_k)$
      $C_k = B_k$
    end if
  end for
Calculate FFT spectrum $x = \mathcal{F}(C_k)$
Output: Detect fault component in x

2) Performance evaluation (synthetic signal)

To show the advantages of the proposed method, a synthetic current signal of an IM with BRB fault has been generated using Eq. (2), with the following parameters: $I = 1$, $f_s = 50.06$ Hz, $s = 0.004$, and $\beta = 0.01$. Fig. 7 demonstrates the performance of the proposed method. The sampling frequency used for generating this signal was $f_m = 10$ kHz, and the signal has been simulated for 10 s. These settings make a real situation, with a fundamental frequency (50.06 Hz) that is not an exact multiple of the frequency resolution of the acquisition process ($\Delta f = 1/t = 0.1$ Hz). Following the procedure of Algorithm I, Fig.7 (a) shows the two orthogonal signals (original and its Hilbert transform). The sign functions of these two signals along with original signal and its Hilbert transform are depicted in Fig.7(b). According to (36), (37), (38) and performing rectification, Fig.7(c) can be produced. Fig.8(a) shows the Fourier spectrum of original synthetic signal. It can be found that the sideband frequencies are buried due to the leakage effects of the fundamental frequency. In contrast, when S-ROAT is applied to this signal, the fault characteristic frequency is demodulated, and the fundamental frequency is shifted to the zero frequency and $4f_s$ (Fig.8 (b) and Fig.8 (c)) while in existing rectification method the fundamental frequency is shifted to the zero frequency and $2f_s$ as shown in Fig.9.

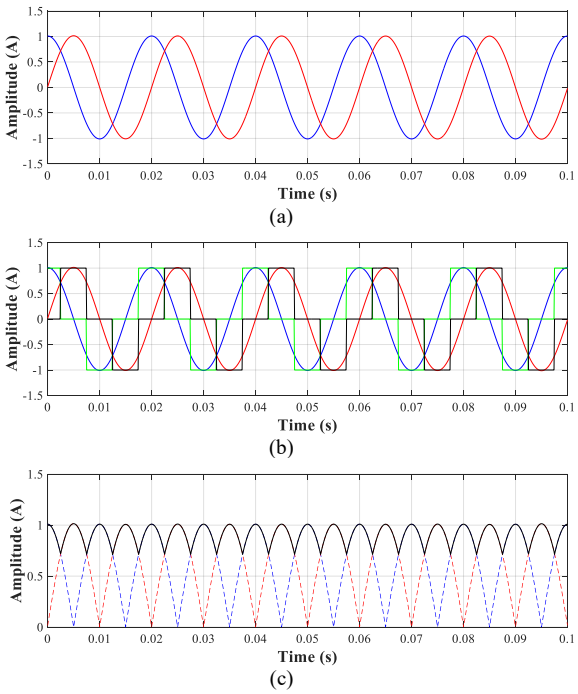

Fig. 7. (a) blue: Synthetic current signal generated with (3) and red: HT synthetic current signal, (b) green: square wave generated with (34) and black: (33) black, (c) black: rectified current (black). f_s = 50.06 Hz, s = 0.004, and β = 0.01.

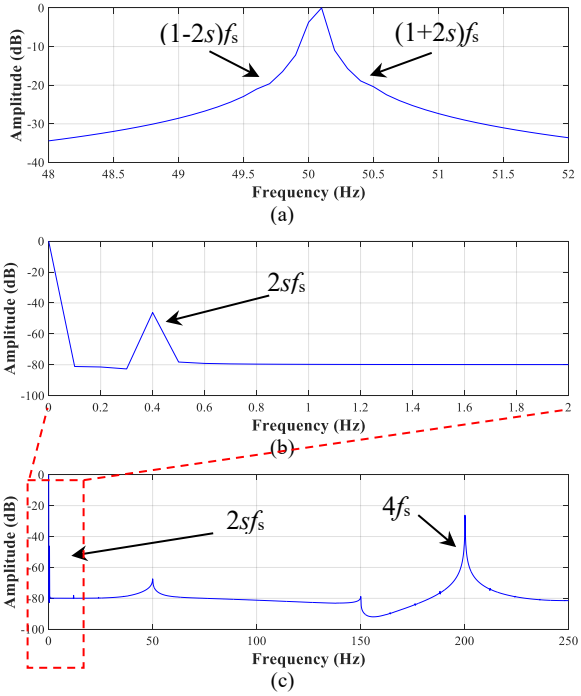

Fig. 8. (a) Fourier transform of the synthetic signal in (36) with f_s = 50.06 Hz, s = 0.004, and β = 0.01, and 10 s with I-BRB – (b)(c) proposed S-ROAT technique.

C. Three Phase Rectified Orthogonal Axes Technique (T-ROAT)

The three-phase version of the ROAT (T-ROAT) is described. The objective is to generate two signals per phase with a 90° phase difference. Consequently, the upper envelope formed by these signals encompasses the fault characteristic frequency ($2sf_s$) and the main harmonic frequency shifted 12 times further. The unique feature of T-ROAT lies in its ability to shift the main harmonic by $12f_s$; however, the inclusion of HT calculations for all three phases increases the complexity.

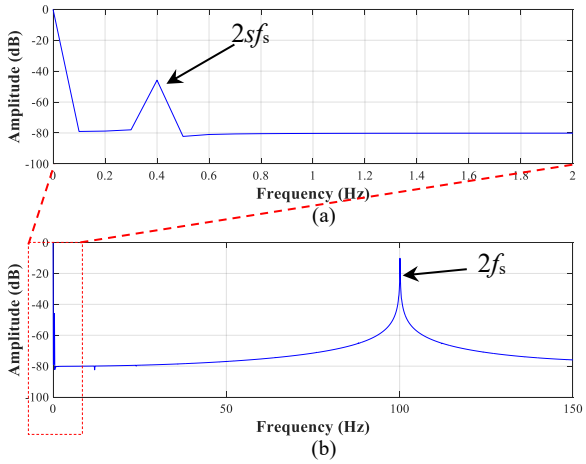

Fig.9. Spectrum of rectified stator current signal.

In the proposed three-phase method, the Hilbert Transform is applied to each phase individually, generating three virtual phases and thus forming a total of six phases (three original and three virtual). Ultimately, rectifying the six phases results in the creation of an upper envelope containing a signal with a frequency twelve times that of the original signal. The mathematical expressions for T-ROAT can be simply expanded by replicating equations given in Section III-B-1.

In order to evaluate the performance of T-ROAT, Fig.10 is provided. Fig.10 (a) shows the two orthogonal signals per phase (original and its Hilbert transform).

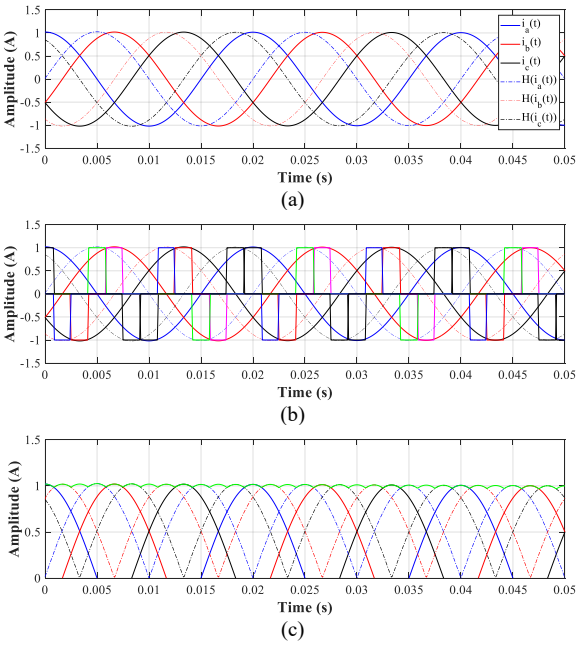

Fig. 10. (a) blue: i_a synthetic signal, red: i_b synthetic signal, black: i_c synthetic signal and dashed line blue: HT [i_a] synthetic signal, dashed line red; HT [i_b] synthetic signal, dashed line black: HT [i_c] synthetic signal, (b) black: square wave generated i_a, green: square wave generated H[i_a], pink: square wave generated i_b, blue: square wave generated H[i_b], orange: square wave generated i_c, gray: square wave generated H[i_c], (c) green: T-ROAT, f_s = 50.05 Hz, s = 0.004, and β = 0.01.

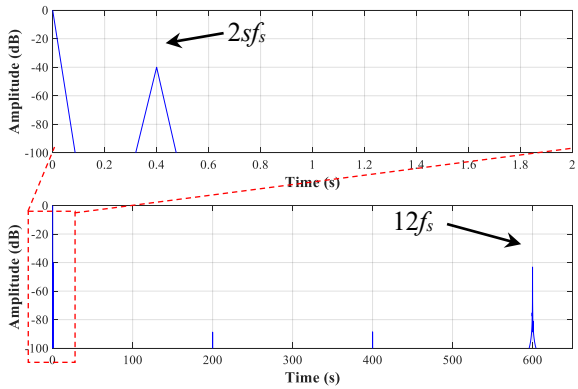

Fig. 11. Fourier transform of the T-ROAT, with f_s = 50.05 Hz, s = 0.004, and β = 0.01, and 10 s, top: 2sf_s, down: 12f_s.

TABLE I
COMPARISON OF DIFFERENT METHODS

Method	No. of sensors	$2sf_s\|_{dB}$	$2sf_s\|_{dB}$
Rectified	1	20log(β/2)	-46.02dB
FDEO	1		
S-ROAT	1		
T-ROAT	3		
EPVA	3		
SAP	3	20log(β)	-39.99dB
TKEO	1		
TOEO	1		
Square	1		

The *sgn* functions of these signals along with original signal and their Hilbert transform are depicted in Fig.10 (b). Similar to the single-phase case, Fig. 10(c) shows the envelope of the sum of the absolute values of all signals, including all three phases and their corresponding Hilbert transforms. When T-ROAT is applied to this signal, the fault characteristic frequency is demodulated, and the fundamental frequency is shifted to the zero frequency and 12f_s (Fig.11 (a) and Fig.11 (b)).

D. Comparison among existing technique

According to Table I, methods such as SAP, TKEO, TOEO, and Square generate the fault characteristic frequency with an amplitude corresponding to twice the actual fault intensity (β). However, the SAP method requires three current sensors. In contrast, methods based on EPVA, FDEO, and rectification display the fault characteristic frequency with an amplitude proportional to the actual fault severity (β/2) (actual value). Notably, the ROAT method is simpler to implement compared to EPVA as it requires only one current sensor instead of three. Additionally, methods utilizing rectified and squared signals generate a fundamental frequency harmonic twice the main frequency (2f_s), positioned close to the fault's characteristic frequency while S-ROAT and T-ROAT shift the fundamental frequency to 4f_s and 12f_s.

IV. EXPERIMENTAL VALIDATION

A. Test-rig description

In squirrel cage induction motors (SCIM), the BRB fault usually occurs due to the complete break of one or more rotor bars. Fig. 12 presents the test-rig of SCIM to validate the effectiveness of the proposed method. The fault analysis was distinct conducted under steady-state mode, encompassing four different scenarios: healthy, one broken rotor bar (I-BRB), two broken rotor bars (II-BRB), and three broken rotor bars (III-BRB). The BRBs are obtained by drilling holes, as shown in Fig. 13. For each conducted test, 25 k samples were used at a sampling frequency of 2 kHz. The supply frequency of the used SCIM was 50 Hz. Table II shows the specifications of the employed SCIM [40].

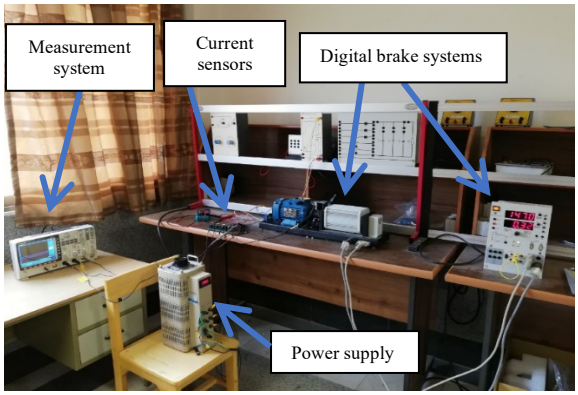

Fig.12.Test-rig of SCIM for diagnosing BRBF.

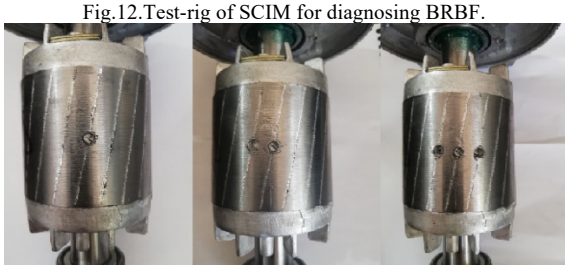

a b c

Fig.13. Faulty rotors- (a) I-BRB, (b) II-BRBs, (c) III-BRBs.

TABEL II
SPECIFICATION OF SCIM

Parameter	Value
Rated voltage (V)	380
Rated power (W)	270
Supply frequency (Hz)	50
Pole pairs	4
Stator winding connections	Y
Stator winding resistance (Ω)	34.73
Rotor cage resistance (Ω)	32.12
Mutual inductance (H)	1.339
Self-inductance of stator (H)	0.139
Self-inductance of rotor (H)	0.159
Inertia (kgm^2)	0.00161

B. Experimental Result

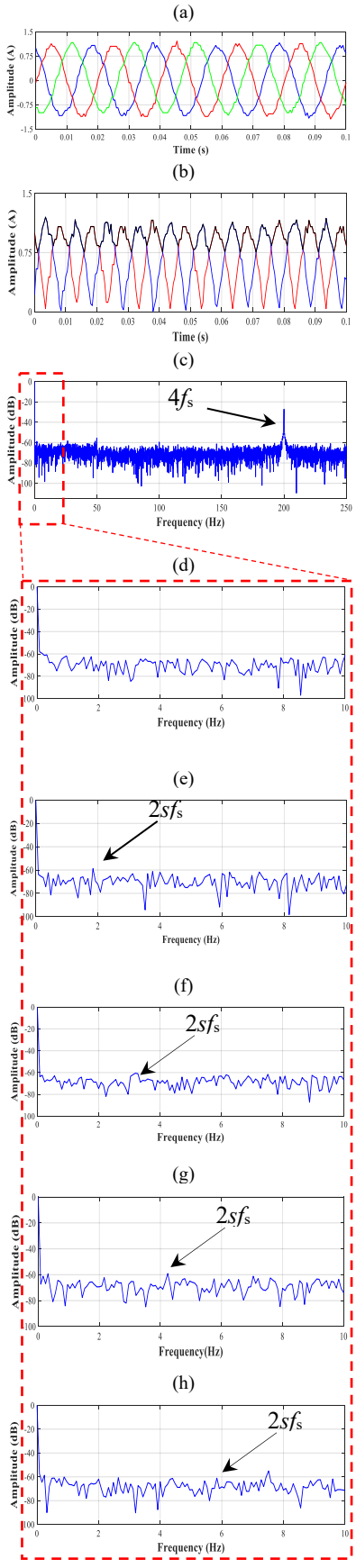

Fig.14. (a) Three phase current signal -(b) signal obtained by the proposed method (black)-(c) spectrum of the proposed method -(d) spectrum of SCIM in healthy condition -(e) the spectrum of the faulty motor (I-BRB) at the rotor speed of 1470 rpm -(f) 1450 rpm -(g) 1430 -(h) 1410 rpm.

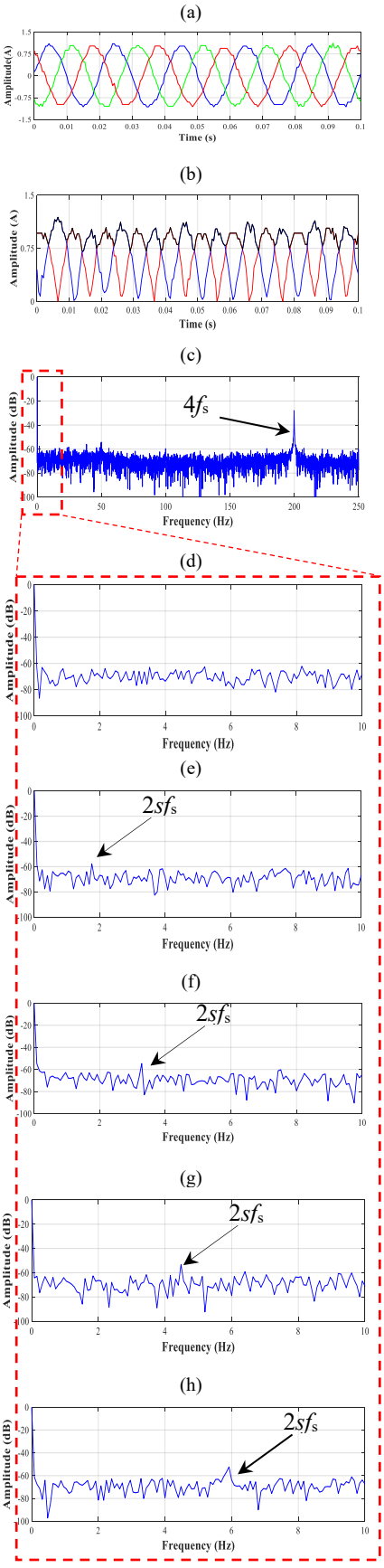

Fig.15. (a) Three phase current signal -(b) signal obtained by the proposed method (black)-(c) spectrum of the proposed method -(d) spectrum of SCIM in healthy condition -(e) the spectrum of the faulty motor (II-BRB) at the rotor speed of 1470 rpm -(f) 1450 rpm -(g) 1430 -(h) 1410 rpm.

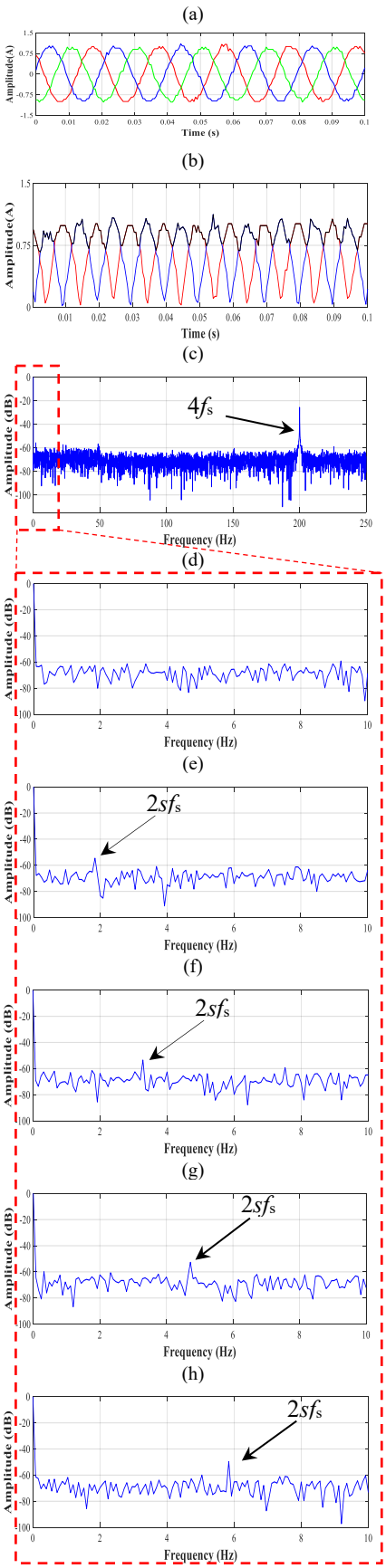

Fig. 16. (a) Three phase current signal -(b) signal obtained by the proposed method (black)-(c) spectrum of the proposed method -(d) spectrum of SCIM in healthy condition -(e) the spectrum of the faulty motor (III-BRB) at the rotor speed of 1470 rpm -(f) 1450 rpm -(g) 1430 -(h) 1410 rpm.

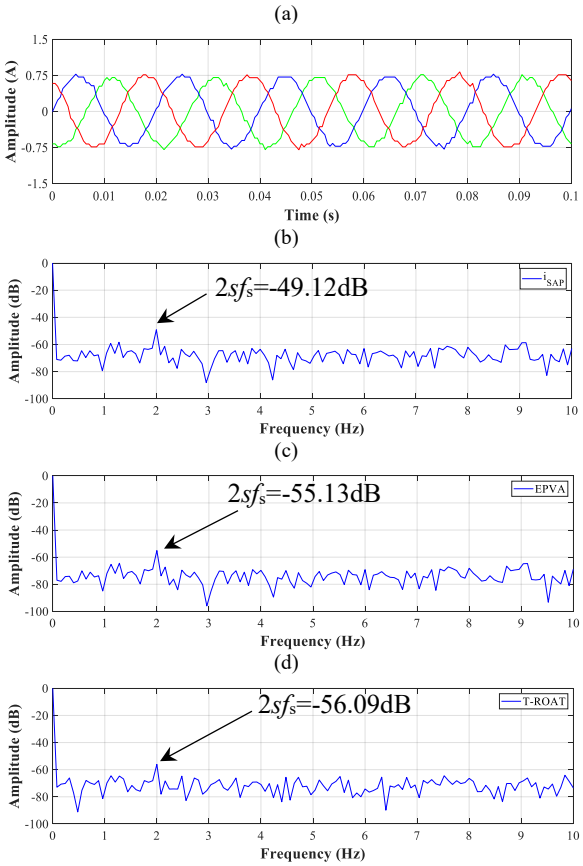

Fig. 17. (a) Three phase current signal of faulty motor (III-BRB) at the rotor speed of 1470 rpm-(b) spectrum of the SAP method -(c) spectrum of the EPVA method -(d) spectrum of the T-ROAT method

The motor has been tested under different speeds and fault severities. The stator current during this period has been recorded for 12.5 s, using a sampling frequency of 2 kHz. Fig. 14, Fig.15 and Fig.16 show the obtained results for I-BRB, II-BRB and III-BRB under different speeds, respectively.
Three-phase current of SCIM is shown in Fig.14 (a), Fig.15(a) and Fig.16 (a). Single phase of SCIM is used to apply the proposed algorithm which has been shown along with HT and the ROAT output (Fig. 14(b), Fig. 15 (b) and Fig. 16 (b)). Fig. 14 (c) - Fig. 14 (g) present the spectra of stator current signature in three different speeds with I-BRB and healthy conditions. Moreover, Fig. 15 and Fig. 16 show the signatures in 3 different speeds with II-BRB and III-BRB.

Comparative experiments of different pervious reported methods which are based on three-phase and single-phase data are given in Fig.17 and Fig.18, respectively. In this regard, frequency spectrums of the stator current for IM with III-BRB at 1470 rpm are obtained. The facts presented in Table I, can be deduced from Fig.17 and Fig.18.

Fig.19 presents the comparison of the amplitude of the fault characteristic frequencies at different BRBs and loads. It is notable that by increasing the number of BRBs, the amplitude of fault characteristic frequency increases. This figure summarizes the performance of ROAT at different speed and fault severities.

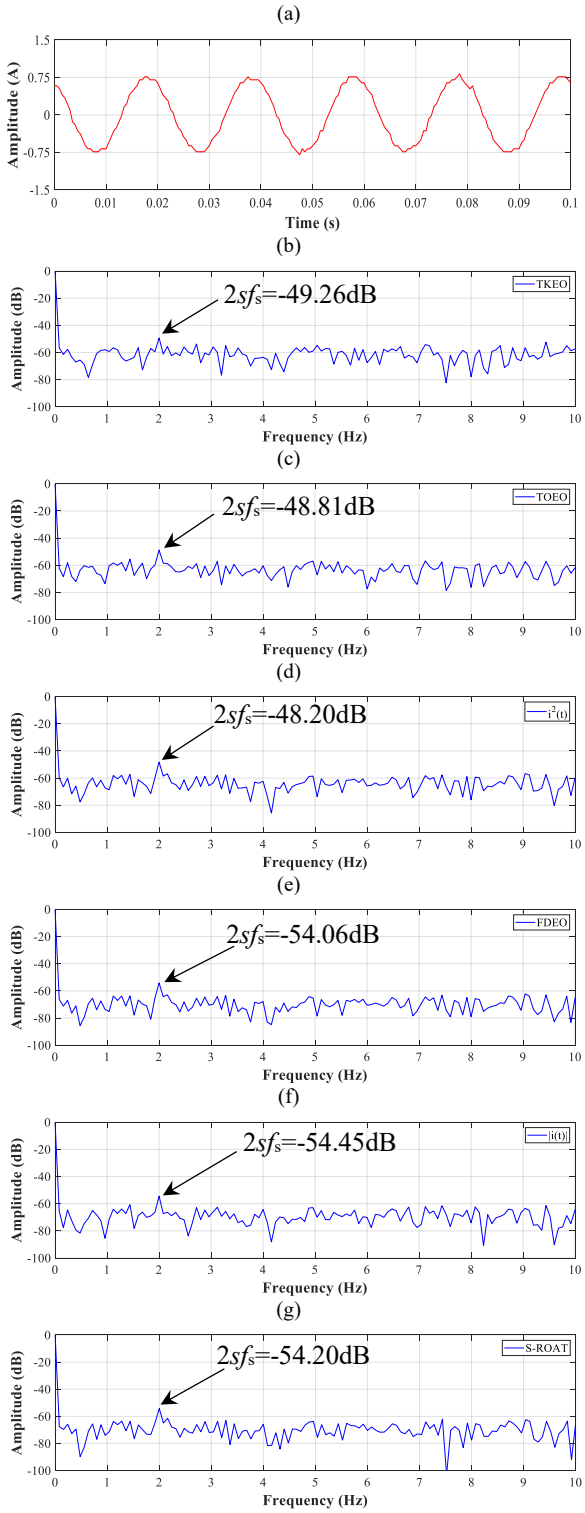

Fig. 18. (a) Single phase current signal of faulty motor (III-BRB) at the rotor speed of 1470 rpm-(b) spectrum of the TKEO method -(c) spectrum of the TOEO method -(d) spectrum of the Square current method-(e) spectrum of the FDEO method -(f) spectrum of the Rectified current method -(g) spectrum of the S-ROAT method

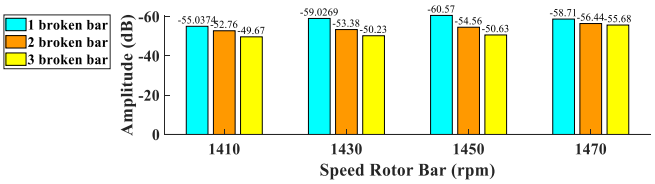

Fig.19. Amplitude of fault characteristic frequency ($2sf_s$) in different load and BRBs.

Moreover, the energy of the fundamental frequency transfers to the DC value and 4th harmonic of the supply frequency. In comparison with rectified stator current signature in which the energy of fundamental frequency transfer to the DC value and 2nd harmonic of supply frequency, the proposed method has better separation.

V. Discussion & Conclusion

This paper introduced a novel technique to detect the BRB fault with the stator single-phase current. The efficacy of the method was validated through both synthetic signals and experimental data containing 1, 2, and 3 broken rotor bars. The proposed method effectively separates the fault-index from the supply frequency, thereby mitigating the adverse effects of main component leakage. Furthermore, it shifts the main harmonic by a factor of 4, doubling effectiveness compared to previous methods. The proposed method proves particularly valuable in scenarios with low amplitude supply frequencies. Our study specifically focused on the accurate demodulation of the fault characteristic frequency components, which is crucial for enhancing fault separability and detection performance in subsequent stages. It can serve as a vital pre-processing step that improves the quality of data fed into data-driven classification techniques, including machine learning and deep learning. By accurately isolating and demodulating these frequency components, our method ensures that the features used by machine learning models are of higher quality and more relevant, thereby potentially increasing the performance of these models. While our current study does not directly apply machine learning or deep learning techniques, it lays a critical foundation for their effective implementation.

The proposed offers a cost-effective and non-invasive approach utilizing existing current sensors and avoiding additional expensive equipment. However, its limitations include sensitivity to electrical noise and disturbances, the complexity of signal processing, partial fault detection, and dependency on load conditions. Our proposed method may also be less effective for certain mechanical faults that do not produce distinct current signatures. Integration with advanced technologies such as machine learning, deep learning, and internet of things (IoT) can enhance detection accuracy and automate diagnostics. Improved signal processing algorithms and hybrid approaches that combine ROAT with other techniques like vibration analysis and thermal imaging can provide more comprehensive fault detection. The use of wireless sensor networks can facilitate the implementation in hard-to-reach or hazardous environments, enabling real-time monitoring and diagnosis.

References

[1] H. Li, G. Feng, D. Zhen, F. Gu and A. D. Ball, "A Normalized Frequency-Domain Energy Operator for Broken Rotor Bar Fault Diagnosis," *IEEE Trans. Instrum. Meas.*, vol. 70, pp. 1-10, 2021.

[2] M. H. Marzebali, S. H. Kia, H. Henao, G. -A. Capolino and J. Faiz, "Planetary Gearbox Torsional Vibration Effects on Wound-Rotor Induction Generator Electrical Signatures," *IEEE Trans. Ind. Appl.*, vol. 52, no. 6, pp. 4770-4780, Nov.-Dec. 2016.

[3] M. H. Marzebali, J. Faiz, G. -A. Capolino, S. H. Kia and H. Henao, "Planetary Gear Fault Detection Based on Mechanical Torque and Stator Current Signatures of a Wound Rotor Induction Generator," *IEEE Trans. Energy Convers.*, vol. 33, no. 3, pp. 1072-1085, Sept. 2018.

[4] M. E. E. -D. Atta, D. K. Ibrahim and M. I. Gilany, "Broken Bar Fault Detection and Diagnosis Techniques for Induction Motors and Drives: State of the Art," *IEEE Access*, vol. 10, pp. 88504-88526, 2022.

[5] V. Abolghasemi, M.H. Marzebali, and S. Ferdowsi, "Recursive singular analysis for induction machines unbalanced rotor fault diagnosis," *IEEE Trans. Instrum. Meas.*, vol. 71, pp. 1–11, 2021.

[6] IEEE Motor Reliability Working Group, "Report of large motor reliability survey of industrial and commercial installations," *IEEE Trans. Ind. Appl.*, vol. IA-21, no. 4, pp. 853–872, Jul. 1986.

[7] K. N. Gyftakis and A. J. M. Cardoso, "Reliable Detection of Stator Interturn Faults of Very Low Severity Level in Induction Motors," *IEEE Ind. Electron. Mag.*, vol. 68, no. 4, pp. 3475-3484, 2021.

[8] M. H. Marzebali, V. Abolghasemi, S. Ferdowsi, and R. Bazghandi, "Manipulation of stator current signature for rotor asymmetries fault diagnosis of wound rotor induction machine," *IET Sci., Meas. Technol.,* vol. 16, no. 9, pp. 523–532, Nov. 2022.

[9] M. H. Marzebali, R. Bazghandi and V. Abolghasemi, "Rotor Asymmetries Faults Detection in Induction Machines Under the Impacts of Low-Frequency Load Torque Oscillation," *IEEE Trans. Instrum. Meas.*, vol. 71, pp. 1-11, 2022.

[10] S. Halder, S. Bhat, D. Zychma, and P. Sowa, "Broken rotor bar fault diagnosis techniques based on motor current signature analysis for induction motor—A review," *Energies*, vol. 15, no. 22, pp. 8569, Nov. 2022.

[11] O. E. Hassan, M. Amer, A. K. Abdelsalam and B. W. Williams, "Induction motor broken rotor bar fault detection techniques based on fault signature analysis—A review", *IET Electr. Power Appl.*, vol. 12, no. 7, pp. 895-907, Aug. 2018.

[12] W. T. Thomson and M. Fenger, "Current signature analysis to detect induction motor faults," *IEEE Ind. Appl. Mag.*, vol. 7, no. 4, pp. 26–34, Jul./Aug. 2001.

[13] O. Guellout, A. Rezig, S. Touati, and A. Djerdir, "Elimination of broken rotor bars false indications in induction machines," Math. Comput. Simul., vol. 167, pp. 250-266, 2020.

[14] S. Kumar, D. Mukherjee, P. K. Guchhait, R. Banerjee, A. K. Srivastava, D. N. Vishwakarma, and R. K. Saket, "A Comprehensive Review of Condition Based Prognostic Maintenance (CBPM) for Induction Motor," *IEEE Access*, vol. 7, pp. 90690–90704, 2019.

[15] V. Climente-Alarcon, J. A. Antonino-Daviu, M. Riera-Guasp, and M. Vlcek, "Induction motor diagnosis by advanced notch FIR filters and the Wigner–Ville distribution," *IEEE Trans. Ind. Electron.*, vol. 61, no. 8, pp. 4217–4227, Aug. 2014.

[16] D. A. Elvira-Ortiz, D. Morinigo-Sotelo, L. Morales-Velazquez, R. A. Osornio-Rios, and R. J. Romero-Troncoso, "Non-linear least squares methodology for suppressing the fundamental frequency in the analysis of electric signals," *Electr. Power Syst. Res.*, vol. 175, Oct. 2019.

[17] M. Abd-el-Malek, A. K. Abdelsalam, and O. E. Hassan, "Induction motor broken rotor bar fault location detection through envelope analysis of start-up current using Hilbert transform*", Mech. Syst. Signal Process.*, vol. 93, pp. 332–350, Sep. 2017.

[18] R. Puche-Panadero, J. Martinez-Roman, A. Sapena-Bano, and J. Burriel Valencia, "Diagnosis of Rotor Asymmetries Faults in Induction Machines Using the Rectified Stator Current," *IEEE Trans. Energy Convers.*, vol. 35, no. 1, pp. 213-221, 2020.

[19] M. Pineda-Sanchez, R. Puche-Panadero, M. Riera-Guasp, J. Perez-Cruz, J. Roger-Folch, J. Pons-Llinares, V. Climente-Alarcon, J. A. Antonino-Daviu, "Application of the Teager-Kaiser Energy

Operator to the Fault Diagnosis of Induction Motors," *IEEE Trans. Energy Convers.*, vol. 28, no. 4, pp. 1036–1044, 2013.

[20] R. Bazghandi, M. H. Marzebali and V. Abolghasemi, "Enhanced Multi-Synchro-Squeezing Transform for Fault Diagnosis in Induction Machine Based on Third-Order Energy Operator of Stator Current Signature," *IEEE Access*, vol. 12, pp. 41056-41065, 2024.

[21] W. Wang, X. Song, G. Liu, Q. Chen, W. Zhao and H. Zhu, "Induction Motor Broken Rotor Bar Fault Diagnosis Based on Third-Order Energy Operator Demodulated Current Signal," *IEEE Trans. Energy Convers*., vol. 37, no. 2, pp. 1052-1059, June 2022.

[22] V. F. Pires, M. Kadivonga, J. Martins and A. Pires, "Motor square current signature analysis for induction motor rotor diagnosis", *Measurement*, vol. 46, pp. 942-948, 2013.

[23] S. M. A. Cruz, A. J. Marques Cardoso, "Rotor Cage Fault Diagnosis in Three-Phase Induction Motors by Extended Park's Vector Approach," Electric Machines & Power Systems, vol. 28, no. 4, pp. 289–299, 2000.

[24] T. A. Garcia-Calva, D. Morinigo-Sotelo, A. Garcia-Perez, D. Camarena- Martinez, and R. de Jesus Romero-Troncoso, "Demodulation technique for broken rotor bar detection in inverter fed induction motor under non-stationary conditions," *IEEE Trans. Energy Convers.*, vol. 34, no. 3, pp. 1496–1503, Sep. 2019.

[25]] R. B. Randall and W. A. Smith, "Uses and mis-uses of energy operators for machine diagnostics," Mech. Syst. Signal Process., vol. 133, p.106, 2019.

[26] H. Li, G. Feng, D. Zhen, F. Gu, and A. D. Ball, "A normalized frequency-domain energy operator for broken rotor bar fault diagnosis," *IEEE Trans. Instrum. Meas*., vol. 70, pp. 1–10, 2021.

[27] I. Boldea and S. A. Nasar, The Induction Machine Handbook, 2nd ed. Boca Raton, FL, USA: CRC Press, 2010, pp. 28–30.

[28] V. Ghorbanian and J. Faiz, "A survey on time and frequency characteristics of induction motors with broken rotor bars in line-start and inverter-fed modes," *Mech. Syst. Signal Process*, vol. 54/55, pp. 427–456, 2015.

[29] P. Wang, K. Wang and L. Chen, "Broken Rotor Bars Detection in Inverter-Fed Induction Motors Under Continuous Switching of Different Speed Modes," *IEEE Trans. Ind. Electron*., vol. 71, no. 1, pp. 975-984, Jan. 2024.

[30] W. S. Abu-Elhaija, V. Ghorbanian, J. Faiz and B. M. Ebrahimi, "Impact of closed-loop control on behavior of inverter-fed induction motors with rotor broken-bars fault," in *Proc. IEEE International Conference on Power Electronics*, Drives and Energy Systems (PEDES), Bengaluru, India, 2012, pp. 1-4.

[31] J. Faiz, V. Ghorbanian, H. Ehya, "Broken bar fault diagnosis in industrial induction motors using the current envelope modulation via TSDM," in *Proc. of the 15th International Conference on Applied Electromagnetics*, NIS, Siberia, 2013.

[32] J. Faiz, V. Ghorbanian, and B. M. Ebrahimi, "Locating Broken Bars in Line-Start and Inverter-Fed Induction Motors Using Modified Winding Function Method," *Electromagnetics*, vol. 32, no. 3, pp. 173-192, 2012.

[33] J. Bonet-Jara, V. Fernandez-Cavero, F. Vedreno-Santos and J. Pons-Llinares, "Very accurate time-frequency representation of induction motors harmonics for fault diagnosis under arbitrary load variations," *International Conference on Electrical Machines* (ICEM), Valencia, Spain, 2022, pp. 1517-1523.

[34] J. Faiz, V. Ghorbanian and B. M. Ebrahimi, "EMD-Based Analysis of Industrial Induction Motors with Broken Rotor Bars for Identification of Operating Point at Different Supply Modes," *IEEE Trans. Ind. Inform.*, vol. 10, no. 2, pp. 957-966, May 2014.

[35] M. Ojaghi, M. Sabouri, J. Faiz, and V. Ghorbanian, "Exact modeling and simulation of saturated induction motors with broken rotor bars fault using winding function approach," *IJE Trans. A, Basics*, vol. 27, no. 1, pp. 69–78, Jan. 2014.

[36] J. Faiz, V. Ghorbanian, B. Ebrahimi, "A survey on condition monitoring and fault diagnosis in line-start and inverter-fed broken bar induction motors," in *Proc*. IEEE International Conference Power Electronics Drives Energy Systems (PEDES), Bengaluru, India, 16–19 December 2012, pp. 1–5.

[37] R. Bazghandi, M. H. Marzebali, V. Abolghasemi, S. H. Kia. A Novel Mode Un-Mixing Approach in Variational Mode Decomposition for Fault Detection in Wound Rotor Induction Machines. *Energies*, vol. 16, no. 14, pp. 5551-5568, 2023.

[38] R. Bazghandi, M. H. Marzebali, V. Abolghasemi, "Asymmetrical Fault detection in induction motors through elimination of load torque oscillations effects in the slight speed variations and steady-state conditions," *IEEE J. Emerg. Sel. Top. Ind. Electron*. 2022, 4, pp. 725–733.

[39] A.D. Poularikas, The Transforms and Applications Handbook; CRC Press LLC: Boca Raton, FL, USA, 2000.

[40] I. -H. Kao, W. -J. Wang, Y. -H. Lai and J. -W. Perng, "Analysis of Permanent Magnet Synchronous Motor Fault Diagnosis Based on Learning," *IEEE Trans. Instrum. Meas*., vol. 68, no. 2, pp. 310-324, Feb. 2019.